

Raman Spectroscopy of Graphene Edges

C. Casiraghi,^{†,‡} A. Hartschuh,[‡] H. Qian,[‡] S. Piscanec,[†] C. Georgi,[‡] A. Fasoli,[†]
K. S. Novoselov,[§] D. M. Basko,^{||} and A. C. Ferrari^{*†}

Engineering Department, Cambridge University, Cambridge, U.K., Chemistry and Biochemistry Department and CeNS, Ludwig-Maximilians- University of Munich, Germany, Department of Physics and Astronomy, Manchester University, U.K., Laboratoire de Physique et Modélisation des Milieux Condensés, Université Joseph Fourier and CNRS, Grenoble, France

Received October 29, 2008; Revised Manuscript Received January 27, 2009

ABSTRACT

Graphene edges are of particular interest since their orientation determines the electronic properties. Here we present a detailed Raman investigation of graphene flakes with edges oriented at different crystallographic directions. We also develop a real space theory for Raman scattering to analyze the general case of disordered edges. The position, width, and intensity of G and D peaks are studied as a function of the incident light polarization. The D-band is strongest for polarization parallel to the edge and minimum for perpendicular. Raman mapping shows that the D peak is localized in proximity of the edge. For ideal edges, the D peak is zero for zigzag orientation and large for armchair, allowing in principle the use of Raman spectroscopy as a sensitive tool for edge orientation. However, for real samples, the D to G ratio does not always show a significant dependence on edge orientation. Thus, even though edges can appear macroscopically smooth and oriented at well-defined angles, they are not necessarily microscopically ordered.

Graphene is the latest carbon allotrope to be discovered, and it is now at the center of a significant experimental and theoretical research effort.^{1–6} In particular, near-ballistic transport at room temperature and high carrier mobilities (between 3000 and 200 000 cm²/Vs)^{5–10} make it a potential material for nanoelectronics,^{11–14} especially for high frequency applications.

Graphene layers can be readily identified in terms of number and orientation by elastic and inelastic light scattering, such as Raman^{15,16,18–20,17} and Rayleigh spectroscopies.^{21,22} Raman spectroscopy also allows monitoring of doping, defects, and strain.^{15,18,23–26}

Once identified, graphene layers can be processed into nanoribbons (GNRs) by lithography.^{1,11,14,27,28} Similar to the case of nanotubes, confinement modifies the electronic structure of graphene, when cut into GNRs^{29–35} The edges of GNRs could in general be a combination of armchair or zigzag regions.^{36–39} If a GNR is uniquely limited by one type of edge, it is defined either as armchair or zigzag.^{29,30,39} Edges are also preferred sites for functionalization with different groups.⁴⁰

Here we show that Raman spectroscopy is a sensitive tool to probe the nature of graphene edges. Our results challenge the suggestion that perfectly armchair or zigzag edges are routinely obtained when exfoliating graphene, even though they appear to follow defined directions on a large scale.

Single layers are produced by microcleavage of graphite. These have areas up to 100 μm² and show sharp edges with different orientations. Raman spectra are measured with a 100× objective at 514, 633, and 488 nm with a Renishaw micro-Raman spectrometer, having a 1800 grooves/mm grating and spectral resolution of ~3 cm⁻¹. The polarization of the incident light can be controlled by a Fresnel rhomb. Raman mapping is performed in another Raman setup based on an inverted confocal microscope at 633 nm. In this case, the beam is reflected by a splitter and focused by an objective with high numerical aperture. The Raman peaks variation across the edge is recorded by raster-scanning the sample with a piezo-stage. The acquisition time per pixel is of the order of few minutes. Gratings of 150 and 600 grooves/mm are used. The spatial resolution is ~800 nm. The power on the samples is well below 2 mW, so that no shift nor change in width of the Raman peaks is observed, thus ensuring no damage nor heating.

All carbons show common features in their Raman spectra in the 800–2000 cm⁻¹ region, the so-called G and D peaks, which lie at around 1580 and 1350 cm⁻¹ respectively.⁴¹ The

* To whom correspondence should be addressed. acf26@eng.cam.ac.uk.

† Cambridge University.

‡ Ludwig-Maximilians- University of Munich.

§ Manchester University.

|| Université Joseph Fourier and CNRS.

† Present address: Physics Department, Free University, Berlin.

G peak corresponds to the E_{2g} phonon at the Brillouin zone center. The D peak is due to the breathing modes of sp^2 rings and requires a defect for its activation.^{42,43} It comes from TO phonons around the \mathbf{K} -point of the Brillouin zone,^{42,43} is active by double resonance (DR),^{44,45} and is strongly dispersive with excitation energy due to a Kohn Anomaly at \mathbf{K} .¹⁹ The activation process for the D peak is intervalley as follows: (i) a laser induced excitation of an electron/hole pair; (ii) electron–phonon scattering with an exchanged momentum $q \sim \mathbf{K}$; (iii) defect scattering; and (iv) electron/hole recombination. The D peak intensity is not related to the number of graphene layers, but only to the amount of disorder.^{42,43} Indeed, when moving from graphite to nanocrystalline graphite, the ratio between the intensity of D and G peak, $I(D)/I(G)$, varies inversely with the size of the crystalline grains or interdefect distance.^{42,43} DR can also happen as intravalley process, that is, connecting two points belonging to the same cone around \mathbf{K} (or \mathbf{K}'). This gives rise to the so-called D' peak, which can be seen around 1620 cm^{-1} in defected graphite.⁴⁶ The 2D peak is the second order of the D peak. This is a single peak in monolayer graphene, whereas it splits in four in bilayer graphene, reflecting the evolution of the band structure.¹⁶ The $2D'$ peak is the second order of the D' peak. Since 2D and $2D'$ peaks originate from a Raman scattering process where momentum conservation is fulfilled by the participation of two phonons with opposite wavevectors (q and $-q$), they do not require defects for their activation and are thus always present.

It is common for as prepared graphene not to have enough structural defects for the D peak to be seen,¹⁶ which is indicative of the high crystallinity of graphene obtained by micromechanical cleavage. In this case, the D peak is only present at the edges,¹⁶ since they act as defects, allowing elastic backscattering of electrons even in an otherwise defect-free sample. It is crucial to distinguish between ordered (zigzag or armchair) and disordered edges. In their seminal work on graphite edges, Cañado et al.^{47,48} have suggested that a perfect zigzag edge cannot activate the D peak due to momentum conservation. Here, we note that a graphene edge is a translationally noninvariant system. Thus we introduce a novel real space representation for Raman scattering in graphene, which allows us to consider the general case of disordered edges. We first consider more closely the nature of the intermediate electronic states involved in the DR process. This starts with the absorption of a photon of energy $\hbar\omega_L$ and the creation of an electron–hole pair (e–h). The one-phonon DR Raman scattering giving rise to the D peak is not a fully resonant process, since at least one of the elementary scattering processes must violate the energy conservation, by an amount of the order of the phonon energy, $\hbar\omega_D \approx 0.17 \text{ eV}$. This means that the photoexcited electron–hole pair is a virtual state (no real electron–hole populations are created), with lifetime determined by the uncertainty principle, of the order of $1/\omega_D \sim 3 \text{ fs}$. This time scale sets the duration of the whole process. Still, as $\hbar\omega_D \approx 0.17 \text{ eV}$ is much smaller than the electron energy ($\varepsilon \approx 1.2 \text{ eV}$ for 514 nm excitation), we will speak about electron and hole energies. Assuming a perfect

symmetry between valence and conduction bands, we can take the energies of the electron and hole, measured from the Dirac point, to be $\varepsilon \approx \hbar\omega_L/2$. Then, again considering that the photon momentum is negligible, the e and h wavevectors measured from \mathbf{K} have modulus $k' = \varepsilon/(\hbar v_F)$, where v_F is the Fermi velocity. The photoexcited electron and hole can also be viewed as wave packets of size $\sim \hbar v_F/\varepsilon$. The time scale $1/\omega_D$ translates into the length scale v/ω_D , where $v \approx 1.1 \times 10^6 \text{ m/s} \approx 7.3 \text{ eV}\cdot\text{\AA}/\hbar$ is the electron velocity (the slope of the Dirac cones). This length scale, $v/\omega_D \approx 4 \text{ nm}$, sets the spatial extent of the process. This is much longer than the electron wavelength $\hbar v/\varepsilon \approx 0.6 \text{ nm}$, ensuring that the wave functions determining the matrix elements for each elementary process admit a quasiclassical representation. This is fully analogous to the geometrical optics approximation for electromagnetic waves. Corrections to this approximation are known as diffraction, and are of order $\hbar\omega_D/\varepsilon \ll 1$. Note that this picture is neither an assumption, nor a hypothesis, but arises automatically in the Raman matrix elements as a consequence of the separation of the two scales given by the energy uncertainty and the energy itself, in analogy to what reported in ref 49 for the fully resonant two-phonon Raman process.

We note that ref 20 reported a measurement of the length over which the Raman process is restricted to the edge. The authors assumed this to be the phase-breaking length, that is, the average distance traveled by an electron before undergoing inelastic scattering by a phonon. As discussed above, to us it seems more natural to associate this length scale with the distance traveled over the lifetime of the virtual electron–hole pair, $v/\omega_D \sim 4 \text{ nm}$. We can also quantify the electron phase-breaking length from the electron–phonon coupling of \mathbf{K} phonons, which was both calculated and compared with different experiments.^{19,50,51} The electron–phonon scattering rate can be written as $2\gamma/\hbar \approx (60 \text{ meV})/\hbar$.⁵² This allows us to estimate the phase-breaking length as $\hbar v/(2\gamma) \approx 11 \text{ nm}$. Since the D peak does not arise exactly from \mathbf{K} phonons, we expect the actual phase-breaking length to be slightly longer. However, the value suggested in ref 20 ($\sim 40 \text{ nm}$) is much bigger. Thus, considering that extracting nanometer length scales from far field Raman measurements, as in ref 20, is extremely challenging and given the lack of a fully quantitative theory, further studies, including near field Raman measurements, are necessary to reach a definite conclusion. In any case, the value of the length reported in ref 20 would further validate our quasiclassical picture.

As discussed above, in the quasiclassical framework the photoexcited electron and hole can be viewed as wave packets of size $\sim \hbar v/\varepsilon \sim 0.6 \text{ nm}$, initially created at an arbitrary point of the sample. More precisely, instead of a point one has to consider a region of length δl , such that $v/\omega_D > \delta l > \hbar v/\varepsilon$. Then, momentum conservation holds up to $\delta q \sim \hbar/\delta l < \varepsilon/v$ by virtue of the uncertainty principle. Thus, electron and hole momenta of magnitude ε/v (from the Dirac point) have approximately opposite directions, since the photon momentum is very small. The same argument holds for phonon emission and for the radiative recombination process; in order to emit a photon, the electron and hole

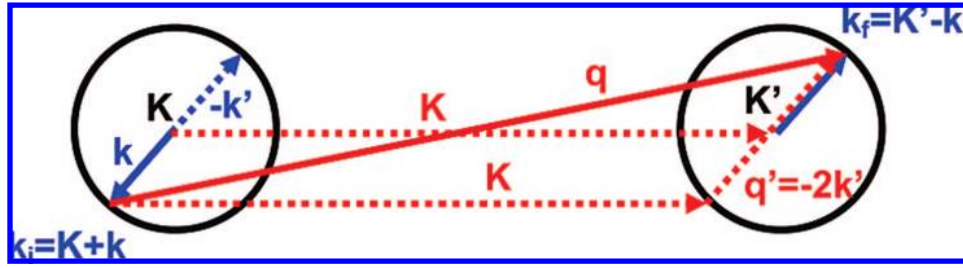


Figure 1. Reciprocal space scheme of the e–h backscattering condition. The circles represent isoenergy cuts on the Dirac cones. A phonon \mathbf{q} (solid red arrow) backscatters an electron from $k_i = \mathbf{K} + \mathbf{k}'$ to $k_f = \mathbf{K}' - \mathbf{k}'$. Since $\mathbf{q} = \mathbf{K} + \mathbf{q}'$, back-scattering happens only if $\mathbf{q}' = -2\mathbf{k}'$. The orientation of the crystal is that shown in Figure 5.

must meet in the same region of space of size δl with almost opposite momenta (up to $\hbar/\delta l$). In the case of the D-peak activation by a generic defect, the events that lead to the e–h recombination are the inelastic scattering with a phonon and the elastic scattering with a defect. Since the recombining e, h have opposite momentum, both phonon and defect scattering have to be back-scattering events.⁴⁹ Thus, to activate a D-peak, phonon scattering has to satisfy two constraints: the first is that the phonon wavevector, \mathbf{q} , must have one end on the Dirac cone around \mathbf{K} and the other on the cone around \mathbf{K}' . The second is set by the back-scattering constraint. This implies that, if \mathbf{k}' and \mathbf{q}' are the electron and phonon wave-vectors measured from \mathbf{K} , we need $\mathbf{q}' = -2\mathbf{k}'$, as for Figure 1. This limits the subset of \mathbf{q} satisfying the first condition. The defect scattering must also satisfy two constraints: momentum conservation in the phonon scattering, and back-scattering. Momentum conservation implies that the momentum exchanged by the defect elastic scattering has to be $\mathbf{d} = -\mathbf{q}$. This implies that the back-scattering condition $\mathbf{d} = \mathbf{K}' + 2\mathbf{k}'$ is automatically satisfied.

Momentum conservation upon reflection from an edge depends on the orientation and quality of the edge and will be discussed below. However, regardless of edge quality, from pure geometric considerations, illustrated in Figure 2, both phonon and edge must scatter electrons backwards. Electrons back-scattered by ordered armchair edges change their momentum by \mathbf{d}_A , while those by ordered zigzag edges by \mathbf{d}_Z , as indicated in Figure 3. Figure 4A shows that \mathbf{d}_A is directed along $\mathbf{K} - \mathbf{K}'$, while \mathbf{d}_Z along $\mathbf{K} - \mathbf{K}$. Since the D peak onset requires scattering between the two nonequivalent cones centered at \mathbf{K} and \mathbf{K}' (intervalley scattering), the D peak cannot be produced by a perfect zigzag edge, while it should appear near a perfect armchair edge, as proposed by refs 47 and 48. This does not apply to the D' peak. Geometrical considerations, illustrated in Figure 4B, show that the D' peak, not involving intervalley scattering, can be activated both by armchair and zigzag edges, since both \mathbf{d}_A and \mathbf{d}_Z are compatible with the required intravalley scattering. This is not enough to determine whether one type of edge is more efficient than the other for the D' activation. This question requires a detailed calculation beyond the scope of the present work.

The backscattering condition has immediate consequences for the polarization dependence of the Raman scattering intensity. Indeed, the matrix element of creation/annihilation of an electron–hole pair with momenta \mathbf{k} , $-\mathbf{k}$ (from the

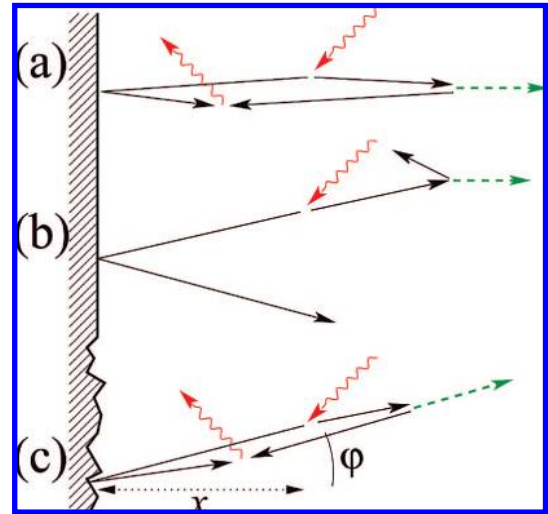


Figure 2. Real space representation of the scattering process for the D peak in the vicinity of an edge. The wavy lines represent the incident photon generating an electron–hole pair, and the scattered photon produced from the pair recombination. The solid black arrows are the quasi-classical trajectories of electron and hole. The dashed arrow is the emitted phonon. (a) Backscattering off an ordered edge is possible only at normal incidence (up to the quantum diffraction correction to the quasiclassical approximation, of order $(\hbar\omega_{\text{ph}}/\epsilon)^{1/2} \ll 1$). (b) For oblique incidence on an ordered edge, reflection is specular, so the electron and hole will not meet at the same point and will not recombine radiatively. (c) For a disordered edge backscattering is possible even at oblique incidence. The typical distance x from the edge is determined by the lifetime of the virtual electron–hole pair, $\sim v/\omega_{\text{ph}}$.

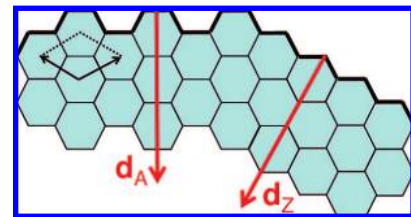


Figure 3. The wavevector direction of electrons back-scattered by a zigzag, or armchair edge (\mathbf{d}_Z , \mathbf{d}_A) is perpendicular to the edge.

Dirac point) by an incident photon with polarization \mathbf{e}_{in} , is proportional to $[\mathbf{e}_{\text{in}} \times \mathbf{k}]$. This is maximum when $\mathbf{e}_{\text{in}} \perp \mathbf{k}$. Since a perfect edge allows momentum conservation along its direction, backscattering is possible only at normal incidence (see Figures 2, 3, and 4C). This gives the polarization dependence of the D intensity $I(D) \propto \cos^2 \theta_{\text{in}}$, Figure 4C, in agreement with refs 47 and 48. More generally,

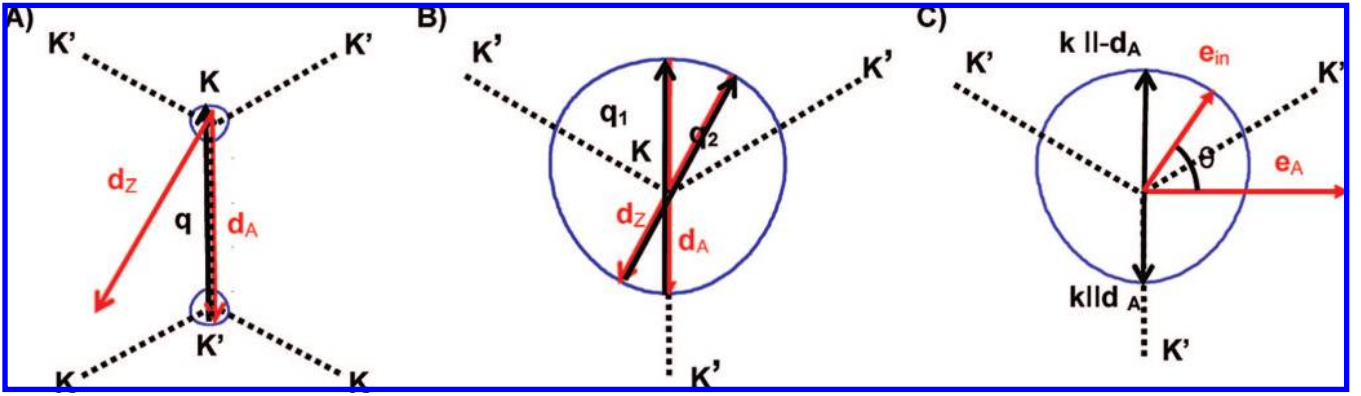


Figure 4. (A) Schematic of intervalley process: only the exchanged momentum from armchair edges \mathbf{d}_A can connect \mathbf{K} and \mathbf{K}' . (B) Schematic of intravalley process: both the exchanged momentum from armchair and zigzag edges, \mathbf{d}_z and \mathbf{d}_A , can connect points belonging to the same region around \mathbf{K} (\mathbf{K}'). The blue line is a iso-energy contour, taking into account the trigonal warping.⁵³ (C) Schematic of polarized Raman: when the incoming light is polarized along \mathbf{e}_{in} , the D intensity depends on θ_{in} , the angle between the incident polarization and the armchair direction (\mathbf{e}_A). The orientation of the crystal is that shown in Figure 3.

calling θ_{in} and θ_{out} the angles formed between the polarizations of incident and scattered photons and the edge, we would get $I(D) \propto \cos^2 \theta_{in} \cos^2 \theta_{out}$. However, in our experiments we collect all the scattered photons without an analyzer, thus we have no dependence on θ_{out} .

We now consider disordered edges. An important characteristic is the length scale ξ over which they are disordered, which may be viewed as a correlation length. If this is significantly larger than the C–C bond length, $a \approx 0.14$ nm, the edge behaves as a collection of locally perfect segments. However, only the armchair segments will contribute to the D peak. First, let us consider a single segment. If its length is large enough, $\xi \gg \hbar v/\varepsilon \approx 0.6$ nm, the electron is reflected almost as if this were a perfect edge, save a small correction due to diffraction. This implies that backscattering is possible not only at normal incidence, but also at small angles $\sim \hbar v/(\varepsilon \xi)$. Thus, the D peak intensity for polarization perpendicular to the local armchair segment direction will be minimum, and smaller than the maximum intensity by a factor $\sim \hbar v/(\varepsilon \xi)$. If the segment is short, $\xi \ll \hbar v/\varepsilon$, it behaves as a short-range impurity. Electron scattering from an arbitrary short-range impurity was considered in ref 54. For impurities with the same symmetry as a \mathbf{K} point phonon (i.e., those which efficiently activate the D peak) the backscattering probability does not depend on the angle of incidence. Thus, for a single very short armchair segment we do not expect polarization dependence.

The most general dependence of D peak intensity on incident photons polarization can be written as

$$I(D)(\theta_{in}) = I(D)_{\min} + [I(D)_{\max} - I(D)_{\min}] \cos^2(\theta_{in} - \theta_{\max}) \quad (1)$$

where $I(D)_{\min}$, $I(D)_{\max}$ are the maximum and minimum D intensities, and θ_{\max} is the angle at which the maximum is measured. This follows from the fact that the Raman intensity is bilinear in the components of the polarization vector. Thus, for a long armchair segment we expect θ_{\max} to correspond to the armchair direction, and $\rho_{A_0} = I(D)_{\min}/I(D)_{\max}$ to be

small. As the length decreases, $\rho_{A_0} \rightarrow 1$, while θ_{\max} always selects the armchair direction.

In general, a disordered edge can contain armchair segments of three orientations.³⁷ If the average direction is armchair, we expect most segments to be oriented along the average direction, and some fraction f at $\pm 60^\circ$. For a random collection of segments, we add the intensities incoherently

$$(1-f)[\rho_{A_0} + (1-\rho_{A_0})\cos^2 \theta_{in}] + (f/2)[\rho_{A_0} + (1-\rho_{A_0})\cos^2(\theta_{in} - 60^\circ)] + (f/2)[\rho_{A_0} + (1-\rho_{A_0})\cos^2(\theta_{in} + 60^\circ)] \quad (2)$$

The resulting ratio is then

$$\rho_A = \frac{\rho_{A_0} + 3f/(4-3f)}{1 + 3f\rho_{A_0}/(4-3f)} \geq \rho_{A_0} \quad (3)$$

and the maximum is at $\theta_{\max} = 0$.

We now consider a disordered edge with an average zigzag orientation. Here, we expect armchair segments at $\pm 30^\circ$ with respect to the average zigzag direction. If the edge is symmetric on the average, they contribute equally; otherwise one of the two directions is favored. Denoting their weights by f_1 and f_2 , we add the intensities as

$$f_1[\rho_{A_0} + (1-\rho_{A_0})\cos^2(\theta_{in} - 30^\circ)] + f_2[\rho_{A_0} + (1-\rho_{A_0})\cos^2(\theta_{in} + 30^\circ)] \quad (4)$$

which gives

$$\rho_Z = \frac{\rho_{A_0} + (2-k)/(2+k)}{1 + \rho_{A_0}(2-k)/(2+k)}, \quad k = \sqrt{1 + 3 \frac{(f_1 - f_2)^2}{(f_1 + f_2)^2}} \quad (5)$$

$$\theta_{\max} = \frac{1}{2} \arctan \frac{\sqrt{3}(f_1 - f_2)}{(f_1 + f_2)} \quad (6)$$

If the edge is on the average symmetric, $f_1 = f_2$, $\theta_{\max} = 0$ and ρ_z is between one-third (long armchair segments) and 1 (short armchair segments).

To summarize, in all cases the presence of short armchair segments with two or three different orientations tends to increase $I(D)_{\min}/I(D)_{\max} \rightarrow 1$ and moves $\theta_{\max} \rightarrow 0$. However, there is another effect which prevents $I(D)_{\min}/I(D)_{\max} \rightarrow 1$. As seen from Figure 2c, if the electron-hole pair is created at a distance x from the edge, and the propagation direction is oblique at an angle φ with respect to the average edge normal direction, this results in a longer path to reach the edge $\propto 1/\cos \varphi$. Since the electron-hole pair lives only a time $\sim 1/\omega_{\text{ph}}$, it has more chance to reach the edge at normal incidence than oblique. This again favors $\theta_{\max} = 0$, but makes $I(D)_{\min}/I(D)_{\max}$ smaller than unity (although a significant fraction of unity). Thus, we expect in general to observe the maximum D peak intensity for polarization parallel to the edge, irrespective of edge orientation and disorder. Should an angle different from zero be measured, this would imply a prevalence of a certain

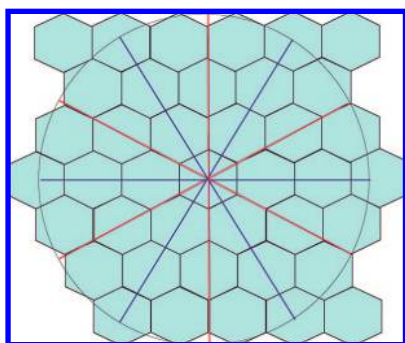


Figure 5. Possible angles formed between two edges. Red lines indicate armchair edges, while blue ones indicate the zigzag edges.

orientation of armchair segments distributed along the average edge direction.

The quasiclassical real space picture for the D' peak is fully analogous to that for the D peak. For regular edges this leads to the same $\cos^2 \theta_{\text{in}}$ polarization dependence of the intensity. To determine the polarization dependence for a disordered edge, one has to add contributions for both armchair and zigzag edges, since they can both be active, but their relative weights are not known. In any case, the presence of segments with different orientations tends to increase $I(D')_{\min}/I(D')_{\max}$ and moves θ_{\max} toward 0.

If we apply the quasiclassical picture to the G peak, we get that this $\mathbf{q} = 0$ phonon cannot change the electron trajectory, so the whole Raman process must occur very quickly in a small region of length $\hbar v/\varepsilon \approx 0.6$ nm at most, which is impossible to resolve with Raman spectroscopy. Thus, only a negligible fraction of the signal from the immediate vicinity of an edge could be affected by its presence, the rest being the bulk G peak, which has no polarization dependence. Thus, we expect the same dependence for $I(D)$ or $I(D)/I(G)$.

We now consider edge identification from optical micrographs. If we examine two edges and assume them ideal, their relative angle would depend only on their nature, as shown in Figure 5, where red lines identify armchair directions and blue identify zigzag directions. For example, if two edges form an angle of 120° , they should be the same. In contrast, an angle of 90° or 150° implies a change (Figure 5). Note that unless the crystallographic orientation of the flake is known a priori or one of the two edges assigned independently, absolute edge assignment is not possible just based on their relative angle.

Figure 6A–C plots the optical micrographs of three samples. They contain single layers, as identified by Rayleigh²¹ and Raman spectroscopy.¹⁶ Figure 6B,D shows samples containing edges forming angles of 90° and 150° , as observed by optical and atomic force microscopy (AFM).

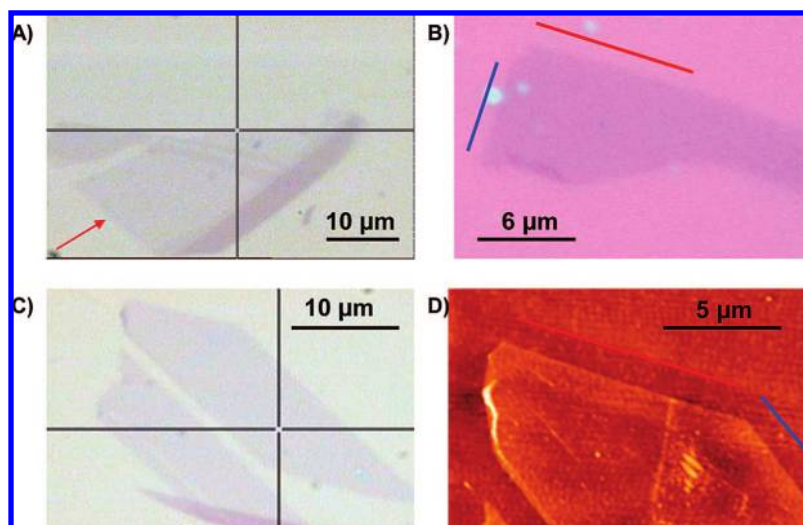


Figure 6. (A) Optical micrograph of the flake used to study a single edge, indicated by the arrow; (B) flake containing two edges at 90° ; (C,D) optical and AFM images of a flake with two edges at an angle of 150° .

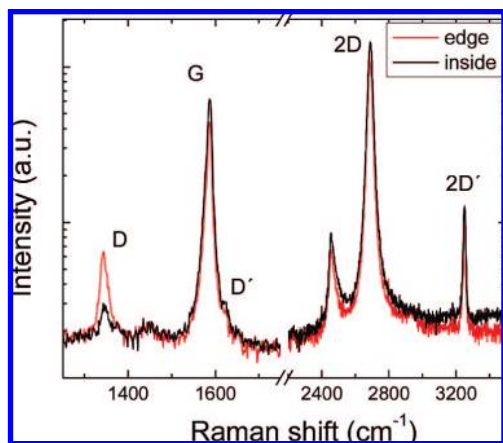


Figure 7. Raman spectra inside the sample (black) and at the edge (red) at 514 nm; a strong D peak is visible at the edge. Note the log scale for the intensity and that the peak at $\sim 1450\text{ cm}^{-1}$ is the third order of the silicon substrate.^{55,56}

Note that these edges appear uniform on a micron length scale.

We first consider the Raman spectra measured at 514 nm for the edge indicated by the arrow in Figure 6A. The edge Raman spectrum, shown in red in Figure 7, has a strong D peak (note the log scale of the y-axis used to enhance the smaller peaks). The peak at $\sim 1450\text{ cm}^{-1}$ in Figure 7 is not due to graphene, since it is visible on the substrate as well, but it is the third order Raman peak of the silicon substrate.^{55–57} The D peak dispersion at the edge is $\sim 50\text{ cm}^{-1}/\text{eV}$, similar to the D peak inside graphite.^{41,58–60} That of the 2D and 2D' peaks is ~ 95 and $\sim 21\text{ cm}^{-1}/\text{eV}$, respectively, as in refs 17 and 61.

Figure 8A plots the spectra for different incident polarization. The D intensity strongly depends on the angle between incident polarization and edge; it is maximum for polarization parallel to the edge and minimum when perpendicular. This agrees with what previously was observed in polarized

measurements at the edge of graphite and graphite ribbons^{47,48} but is here measured on a single graphene layer. Figure 8B shows $I(D)/I(G)$ as a function of θ_{in} for the edge in Figure 6A. The D intensity is consistent with a $\cos^2(\theta_{in})$ dependence; however, it does not go to zero for light polarized perpendicular to the edge (Figure 8). The residual $I(D)/I(G)$ at the edge is ~ 0.14 , larger than in the bulk where $I(D)/I(G) < 0.1$. The ratio of the residual intensity $I(D)_{min}$ to the maximum intensity $I(D)_{max}$, $I(D)_{min}/I(D)_{max} \sim 0.2$. From eqs 3 and 5, this is compatible with the case of an edge with average armchair direction and with armchair segments (i) longer than $\hbar v_F/\epsilon$, and (ii) oriented predominantly along the edge average direction. We then consider a sample with edges oriented at 90° , one respect to the other, similar to Figure 6B. Repeating the same procedure on the two edges we find the results in Figure 9. In this case one of the two edges shows $I(D)_{min}/I(D)_{max} \sim 0.2$ and $\theta_{max} \sim 0$, while the other has $I(D)_{min}/I(D)_{max} \sim 0.35$ and a near zero $\theta_{max} \sim 7^\circ$. It would be thus tempting to assign the first to an edge with average armchair direction and the second to an edge with average zigzag direction but with relatively long armchair segments and not fully symmetric. As discussed later, these cannot be taken as general findings. However, in all the samples we examined, we found the maximum D peak intensity for incident polarization parallel (or near-parallel) to the average edge direction.

To understand how the intensity of the G, 2D and D peaks changes when crossing an edge, Raman mapping is performed with light polarized parallel to the edge direction. Figures 10 show a map of $I(G)$, $I(D)$, $I(2D)$, $I(D)/I(G)$ across the edge. The D peak is localized at the edge, unlike the G peak, which increases, as expected, when moving from outside to inside the sample. Figure 11 plots the profile of $I(G)$, $I(2D)$, $I(D)$ and $I(D)/I(G)$ across the edge. When going from outside to inside the flake, $I(D)$ increases, reaches a maximum and then decreases. Fitting this variation with a Gaussian, we get a width of $\sim 700\text{ nm}$, comparable with our

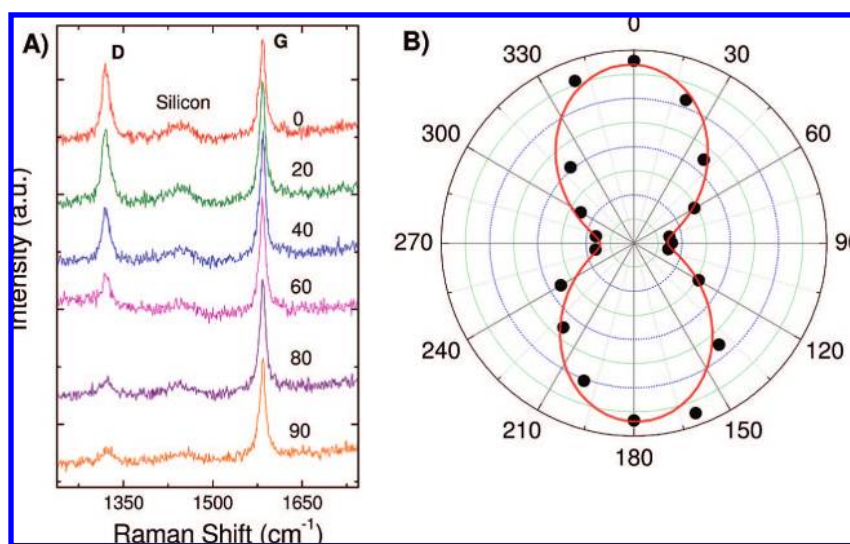


Figure 8. (A) Raman spectra of one edge measured for different incident polarization at 633 nm. (B) $I(D)/I(G)$ as a function of θ_{in} . Note that $I(D)/I(G)$ does not go to zero for perpendicular polarization. This indicates that the edges are not perfect. Red line is the fitting curve according to eq 1, giving $I(D)/I(G) = 0.14 + (0.74 - 0.14)\cos^2(\theta_{in})$.

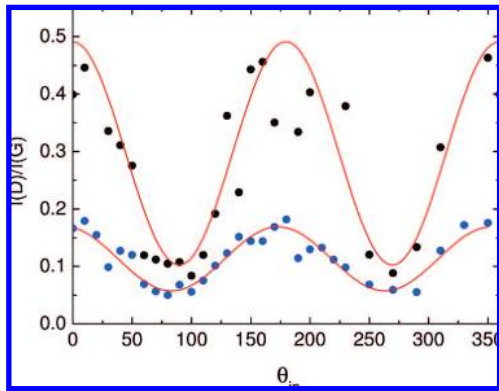


Figure 9. $I(D)/I(G)$ as a function of θ_{in} measured on two edges forming an angle of 90° . Note that $I(D)/I(G)$ does not go to zero for perpendicular polarization in both directions. This indicates that both edges are not perfect. Red lines are fits to the data according to eq 1. These give $I(D)/I(G) = 0.1 + (0.49 - 0.1)\cos^2(\theta_{in})$ for the top black data points and $I(D)/I(G) = 0.06 + (0.17 - 0.06)\cos^2(\theta_{in} - 7^\circ)$ for the bottom blue data points

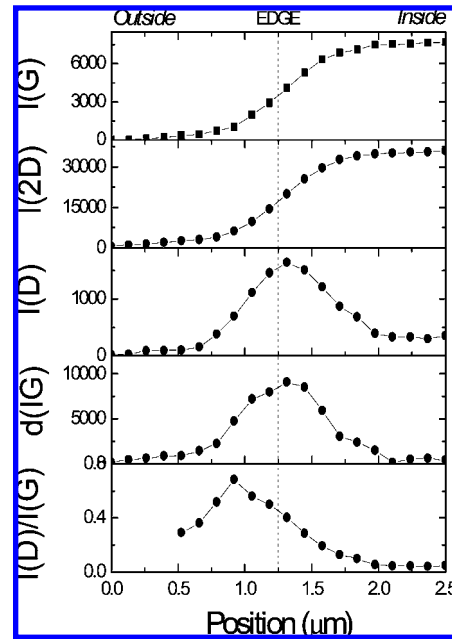


Figure 11. Profile variation of the intensity of G, 2D, D, derivative of the G peak, $d(I(G))$, and $I(D)/I(G)$, measured along the white arrow in Figure 10.

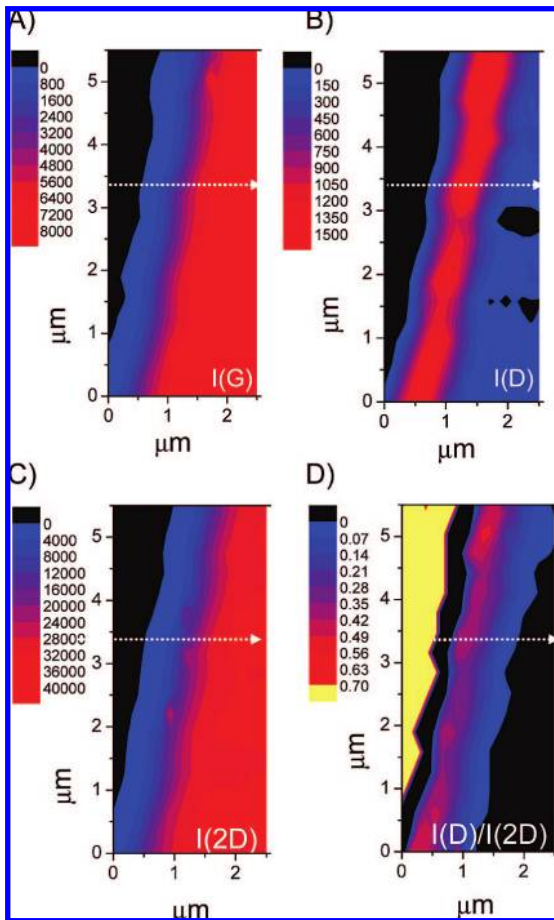


Figure 10. (A) Raman map of $I(G)$ in proximity of the edge shown in red in Figure 6A; (B) Raman map of $I(D)$; (C) Raman map of $I(2D)$; (D) Raman map of $I(D)/I(2D)$. Measurements are taken for incident polarization parallel to the average edge direction

spatial resolution. On the other hand, $I(G)$ decreases moving from inside to outside the flake. This is expected since the Raman intensity of the allowed peak is proportional to the volume of the sample. The same is observed for the 2D peak (Figures 10 and 11).

The D peak behaves in a different way compared to the G and 2D, because its intensity is proportional to the amount of defects, which, neglecting structural disorder, can be assumed to be proportional to the edge length under the laser spot, as discussed above. Thus, the maximum $I(D)$ should be measured when the diameter of the laser beam crosses the edge (dotted vertical line in Figure 11). Here, $I(G)$ is roughly half of $I(G)$ inside the flake. We define this position as the “edge”. Thus, when we refer to any Raman parameter as measured at the edge, we mean measured at this position. This is needed to safely compare values of $I(D)/I(G)$ measured on different edges or different points on the same edge.

Figure 12A shows the Raman spectra obtained when scanning across an edge. We detect a small red shift of the G peak when the laser spot is almost outside the flake, accompanied by a $FWHM(G)$ decrease (Figure 12B). This is not due to increasing disorder, since in this case we expect $FWHM(G)$ to increase,¹⁵ but it could be related to a doping variation,^{15,18,24} that is, this edge shows a slightly higher doping level compared to the bulk. Figure 12B also plots the D peak position. It decreases from 1348 to 1346 cm^{-1} when moving from inside to the edge. This variation is very small, within the spectrometer resolution, and in the opposite direction compared to the G peak. Thus, stress is not the reason of this G peak trend.^{25,26} However, not all the measured edges show this trend, and a more systematic investigation is needed.

Finally, we perform a Raman map on two edges forming angles of 90 and 150° , similar to Figure 6(B,C). This angle implies, for ideal edges, that if one edge is zigzag the other must be armchair or vice-versa, but the two edges cannot have the same chirality, as shown in Figure 5. Unlike the single point measurements of Figures 8 and 9, here we try

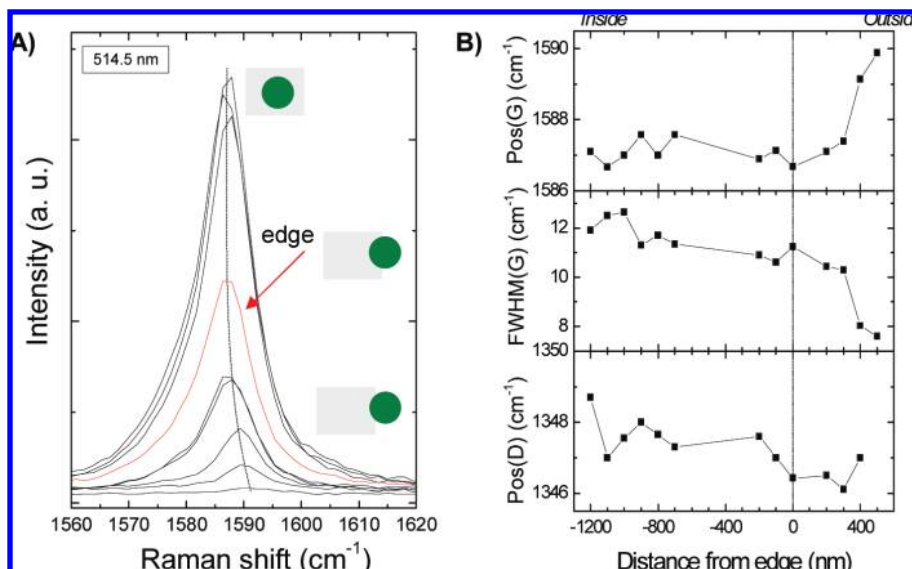


Figure 12. (A) Raman spectra measured at 514 nm across an edge. The green circle represents the laser spot and the gray square is the graphene; (B) G, D peak positions, Pos(D), Pos(G), and FWHM(G) as a function of the distance from the edge.

to capture the response of the entire sample. However, if we mapped the sample with a fixed polarization, as done in the single edge maps in Figure 10, we would preferentially enhance the D peak response of one of the two edges. Thus, we do Raman mapping with circular polarization. Figures 13(A,B) shows the maps of $I(D)$ and $I(D)/I(G)$. No strong variation of $I(D)$ is detected at the edges (Figure 13A); $I(D)/I(G)$ is never null (Figure 13B) in contrast to what expected for ideal zigzag edges. Thus, in this case, the circular polarization maps do not allow to conclusively assign the edges orientation.

It is interesting to compare our data with those in ref 47

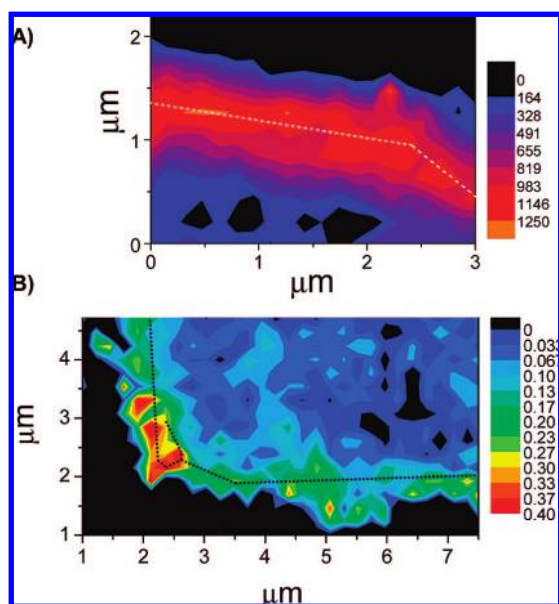


Figure 13. (A) Raman map of $I(D)$ for two edges forming an angle of 150° . $I(D)$ does not show strong variation along the two edges. (B) Raman map of $I(D)/I(G)$ in proximity of two edges forming an angle of 90° . $I(D)/I(G)$ is never null, nor comparable with that inside the flake.

for two graphite edges with an angle of 150° . Reference 47 states that $I(D)$ at the edge is never null due to disorder. However, they claim that a small $I(D)/I(G)$ can be taken as a signature of zigzag edges, while a large $I(D)/I(G)$ indicates armchair edges. This is not the case, as we have discussed above, and only an accurate analysis of the polarization dependence could derive the average edge orientation. Furthermore, the case of a graphite edge, consisting of multiple fractured graphene layers, is much more complex to analyze than a single graphene layer. The D peak intensity should always be maximum along the graphite edge, in agreement with the measurements of ref., 47, but this alone is not sufficient to confirm the average edge orientation. Indeed, here we find that none of the samples we analyzed have perfect edges on a microscopic scale, even though they look very smooth by optical microscopy. In particular, we never observe perfect zigzag edges since our measured $I(D)$ is never null.

In conclusion, Raman spectroscopy is an ideal tool to probe graphene edges. We have developed a real space theory for Raman scattering to analyze the general case of disordered edges. The D to G peak ratio strongly depends on polarization, relative position of the laser spot with respect to the edge, and amount of edge disorder. In some samples, Raman mapping with circular polarization shows no significant dependence of the D peak intensity on the macroscopic edge orientation. This indicates that edges can be mixed and disordered at least on the laser spot scale even though they follow well defined crystallographic directions at a larger scale.

Acknowledgment. We acknowledge L. C. Cançado, P.H. Tan, and S. Reich for useful discussions and A. Lombardo, A. Bonetti, and V. Scardaci for assistance with the samples. C.C. acknowledges the Oppenheimer and the Alexander von Humboldt Foundation, ACF the Royal Society, and the European Research Council Grant NANOPOTS.

References

- (1) Novoselov, K. S.; Geim, A. K.; Morozov, S. V.; Jiang, D.; Zhang, Y.; Dubonos, S. V.; Grigorieva, I. V.; Firsov, A. A. *Science* **2004**, *306*, 666.
- (2) Geim, A. K.; Novoselov, K. S. *Nat. Mater.* **2007**, *6*, 183.
- (3) Castro Neto, A. H.; Guinea, F. Peres, N. M. R.; Novoselov, K. S.; Geim, A. K. arXiv:0709.1163v1.
- (4) Charlier, J. C.; Eklund, P. C.; Zhu, J.; Ferrari, A. C. *Top. Appl. Phys.* **2008**, *111*, 673.
- (5) Novoselov, K. S.; Geim, A. K.; Morozov, S. V.; Jiang, D.; Katsnelson, M. I.; Grigorieva, I. V.; Dubonos, S. V.; Firsov, A. A. *Nature (London)* **2005**, *438*, 197.
- (6) Zhang, Y.; Tan, Y. W.; Stormer, H. L.; Kim, P. *Nature (London)* **2005**, *438*, 201.
- (7) Novoselov, K. S.; Jiang, Z.; Zhang, Y.; Morozov, S. V.; Stormer, H. L.; Zeitler, U.; Maan, J. C.; Boebinger, G. S.; Kim, P.; Geim, A. K. *Science* **2007**, *315*, 1379.
- (8) Morozov, S. V.; Novoselov, K. S.; Katsnelson, M. I.; Schedin, F.; Elias, D. C.; Jaszczak, J. A.; Geim, A. K. *Phys. Rev. Lett.* **2008**, *100*, 016602.
- (9) Du, X.; Skachko, I.; Barker, A.; Andrei, E. Y. *Nat. Nanotechnol.* **2008**, *491*, 3.
- (10) (a) Bolotin, K. I.; Sikes, K. J.; Hone, J.; Stormer, H. L.; Kim, P. *Phys. Rev. Lett.* **2008**, *101*, 096802. (b) Bolotin, K. I.; Sikes, K. J.; Jiang, Z.; Fundenberg, G.; Hone, J.; Kim, P.; Stormer, H. L. *Solid State Commun.* **2008**, *146*, 351.
- (11) Han, M. Y.; Oezylmaz, B.; Zhang, Y.; Kim, P. *Phys. Rev. Lett.* **2007**, *98*, 206805.
- (12) Chen, Z.; Lin, Y. M.; Rooks, M.; Avouris, P. *Physica E* **2007**, *40*, 228.
- (13) Zhang, Y.; Small, J. P.; Pontius, W. V.; Kim, P. *Appl. Phys. Lett.* **2005**, *86*, 073104.
- (14) Lemme, M. C.; Echtermeyer, T. J.; Baus, M.; Kurz, H. *IEEE Electron Device Lett.* **2007**, *28*, 4.
- (15) Casiraghi, C.; Pisana, S.; Novoselov, K. S.; Geim, A. K.; Ferrari, A. C. *Appl. Phys. Lett.* **2007**, *91*, 233108.
- (16) Ferrari, A. C.; Meyer, J. C.; Scardaci, V.; Casiraghi, C.; Lazzeri, M.; Mauri, F.; Piscanec, S.; Jiang, D.; Novoselov, K. S.; Roth, S.; Geim, A. K. *Phys. Rev. Lett.* **2006**, *97*, 187401.
- (17) Malard, L. M.; Nilsson, J.; Elias, D. C.; Brant, J. C.; Plentz, F.; Alves, E. S.; Castro Neto, A. H.; Pimenta, M. A. *Phys. Rev. B* **1999**, *76*, 201401.
- (18) Pisana, S.; Lazzeri, M.; Casiraghi, C.; Novoselov, K. S.; Geim, A. K.; Ferrari, A. C.; Mauri, F. *Nat. Mat.* **2007**, *6*, 198.
- (19) Piscanec, S.; Lazzeri, M.; Mauri, F.; Ferrari, A. C.; Robertson, J. *Phys. Rev. Lett.* **2004**, *93*, 185503.
- (20) Cançado, L. G.; Beams, R.; Novotny, L. arXiv:0802.3709v1 [cond-mat.mtrl.sci].
- (21) Casiraghi, C.; Hartschuh, A.; Lidorikis, E.; Qian, H.; Harutyunyan, H.; Gokus, T.; Novoselov, K. S.; Ferrari, A. C. *Nano. Lett.* **2007**, *7*, 2711.
- (22) Blake, P.; Hill, E. W.; Castro Neto, A. H.; Novoselov, K. S.; Jiang, D.; Yang, R.; Booth, T. J.; Geim, A. K. *Appl. Phys. Lett.* **2007**, *91*, 063124.
- (23) Ferrari, A. C. *Solid State Commun.* **2007**, *143*, 47.
- (24) Das, A.; Pisana, S.; Piscanec, S.; Chakraborty, B.; Saha, S. K.; Waghmare, U. V.; Yang, R.; Krishnamurthy, H. R.; Geim, A. K.; Ferrari, A. C.; Sood, A. K. *Nat. Nanotechnol.* **2008**, *3*, 210.
- (25) Ferralis, N.; Maboudian, R.; Carraro, C. *Phys. Rev. Lett.* **2008**, *101*, 156801.
- (26) Mohiuddin, T. M. G.; Lombardo, A.; Nair, R. R.; Bonetti, A.; Savini, G.; Jalil, R.; Bonini, N.; Basko, D. M.; Galiotis, C.; Marzari, N.; Novoselov, K. S.; Geim, A. K.; Ferrari, A. C. arXiv:0812.1538.
- (27) Lu, X.; Huang, H.; Nemchuk, N.; Ruoff, R. S. *Appl. Phys. Lett.* **1999**, *75*, 193.
- (28) Chen, Z. H.; Lin, Y.-M.; Rooks, M. J.; Avouris, P. *Physica E* **2007**, *40*, 228.
- (29) Nakada, K.; Fujita, M.; Dresselhaus, G.; Dresselhaus, M. S. *Phys. Rev. B* **1996**, *54*, 17954.
- (30) Fujita, M.; Wakabayashi, K.; Nakada, K.; Kusakabe, K. *J. Phys. Soc. Jpn.* **1996**, *65*, 1920.
- (31) Miyamoto, Y.; Nakada, K.; Fujita, M. *Phys. Rev. B* **1999**, *59*, 9858.
- (32) Wakabayashi, K.; Fujita, M.; Ajiki, H.; Sigrist, M. *Phys. Rev. B* **1999**, *59*, 8271.
- (33) Son, Y. W.; Cohen, M. L.; Louie, S. G. *Phys. Rev. Lett.* **2006**, *97*, 216803.
- (34) Pisani, L.; Chan, J. A.; Montanari, B.; Harrison, N. M. *Phys. Rev. B* **2007**, *75*, 064418.
- (35) Nakada, K.; Igami, M.; Fujita, M. *J. Phys. Soc. Jpn.* **1998**, *67*, 2388.
- (36) Niimi, Y.; Matsui, T.; Kambara, H.; Tagami, K.; Tsukada, M.; Fukuyama, H. *Phys. Rev. B* **2006**, *73*, 085421.
- (37) Kobayashi, Y.; Fukui, K.; Enoki, T.; Kusakabe, K.; Kaburagi, Y. *Phys. Rev. B* **2005**, *71*, 193406.
- (38) Sols, F.; Guinea, F.; Castro Neto, A. H. *Phys. Rev. Lett.* **2007**, *99*, 166803.
- (39) Niimi, Y.; Matsui, T.; Kambara, H.; Tagami, K.; Tsukada, M.; Fukuyama, H. *Appl. Surf. Sci.* **2005**, *241*, 43.
- (40) Cervantes, F.; Piscanec, S.; Csanyi, G.; Ferrari, A. C. *Phys. Rev. B* **2008**, *77*, 165427.
- (41) Ferrari, A. C.; Robertson, J. *Phil. Trans. R. Soc. London, Ser. A* **2004**, *362*, 2267-2565.
- (42) Tuinstra, F.; Koenig, J. L. *J. Chem. Phys.* **1970**, *53*, 1126.
- (43) (a) Ferrari, A. C.; Robertson, J. *Phys. Rev. B* **2000**, *61*, 14095. (b) Ferrari, A. C.; Robertson, J. **2001**, *64*, 075414.
- (44) Baranov, A. V.; Bekhterev, A. N.; Bobovich, Y. S.; Petrov, V. I. *Opt. Spektrosk.* **1987**, *62*, 1036.
- (45) Thomsen, C.; Reich, S. *Phys. Rev. Lett.* **2000**, *85*, 5214.
- (46) Nemanich, R. J.; Solin, S. A. *Phys. Rev. B* **1979**, *20*, 392.
- (47) Cançado, L. G.; Pimenta, M. A.; Neves, B. R. A.; Dantas, M. S. S.; Jorio, A. *Phys. Rev. Lett.* **2004**, *93*, 247401.
- (48) Cançado, L. G.; Pimenta, M. A.; Neves, B. R. A.; Medeiros-Ribeiro, G.; Enoki, T.; Kobayashi, Y.; Takai, K.; Fukui, K.; Dresselhaus, M. S.; Saito, R.; Jorio, A. *Phys. Rev. Lett.* **2004**, *93*, 047403.
- (49) Basko, D. M. *Phys. Rev. B* **2008**, *78*, 125418.
- (50) Basko, D. M.; Aleiner, I. L. *Phys. Rev. B* **2008**, *77*, 041409(R).
- (51) Lazzeri, M.; Attacalite, C.; Wirtz, L.; Mauri, F. *Phys. Rev. B* **2008**, *78*, 081406(R).
- (52) Basko, D. M. *Phys. Rev. B* **2007**, *76*, 081405(R).
- (53) Kurti, J.; Zolyomi, V.; Gruneis, A.; Kuzmany, H. *Phys. Rev. B* **2002**, *65*, 165433.
- (54) Basko, D. M. *Phys. Rev. B* **2008**, *78*, 115432.
- (55) Casiraghi, C.; Ferrari, A. C.; Robertson, J.; Ohr, R.; Gradowski, M.; Schneider, D.; Hilgers, H. *Diamond Relat. Mater.* **2004**, *13*, 1480.
- (56) Acker, W. P.; Leach, B. Y., D. H.; Chang, R. K. *J. Appl. Phys.* **1988**, *64*, 2263.
- (57) Temple, P. A.; Hathaway, C. E. *Phys. Rev. B* **1973**, *7*, 3685.
- (58) Pócsik, I.; Hundhausen, M.; Koós, M.; Ley, L. *J. Non-Cryst. Solids* **1998**, *227*, 53.
- (59) Wang, Y.; Alsmeyer, D. C.; McCreery, L. *Chem. Mater.* **1990**, *2*, 557.
- (60) Matthews, M. J.; Pimenta, M. A.; Dresselhaus, G.; Dresselhaus, M. S.; Endo, M. *Phys. Rev. B* **1999**, *59*, R6585.
- (61) Tan, P. H.; Hu, C. Y.; Dong, J.; Shen, W. C.; Zhang, B. F. *Phys. Rev. B* **2001**, *64*, 214301.

NL8032697